UHASSELT
KNOWLEDGE IN ACTION

Maastricht University

Faculty of Medicine and Life Sciences
School for Life Sciences
Master of Biomedical Sciences

Master's thesis

Electrochemical Impedance Spectroscopy biosensor for antigen-antibody detection

Osamah Abd El Motleb Omar

Thesis presented in fulfillment of the requirements for the degree of Master of Biomedical Sciences, specialization Bioelectronics and Nanotechnology

SUPERVISOR :
Prof. dr. ir. Ronald THOELEN

MENTOR :
ing. Seppe BORMANS

2020
2021

Transnational University Limburg is a unique collaboration of two universities in two countries: the University of Hasselt and Maastricht University.

UHASSELT
KNOWLEDGE IN ACTION

www.uhasselt.be
Universiteit Hasselt
Campus Hasselt:
Martelarenlaan 42 | 3500 Hasselt
Campus Diepenbeek:
Agoralaan Gebouw D | 3590 Diepenbeek

UHASSELT
KNOWLEDGE IN ACTION

Maastricht University

Faculty of Medicine and Life Sciences
School for Life Sciences
Master of Biomedical Sciences

Master's thesis

Electrochemical Impedance Spectroscopy biosensor for antigen-antibody detection

Osamah Abd El Motleb Omar

Thesis presented in fulfillment of the requirements for the degree of Master of Biomedical Sciences, specialization Bioelectronics and Nanotechnology

SUPERVISOR :

Prof. dr. ir. Ronald THOELEN

MENTOR :

ing. Seppe BORMANS

Electrochemical Impedance Spectroscopy biosensor for antigen-antibody detection.*

Osamah Abd El Motleb Omar[1], Seppe Bormans[2,3], Thijs Vandenryt[2,3], Ronald Thoelen[2,3]

1. UHasselt, Faculty of medicine and life sciences, Agoralaan, B-3500 Hasselt
2. Institute for Material Research (IMO), Hasselt University, 3500 Hasselt, Belgium
3. IMEC vzw, Division IMOMEC, Wetenschapspark 1, B-3590 Diepenbeek

*Running title: *EIS biosensor for biomolecule detection.*

To whom correspondence should be addressed: Prof. dr. ir. Ronald Thoelen, Tel: +32 (11) 26 88 29; Email: ronald.thoelen@uhasselt.be

Keywords: EIS immunosensor; ELISA protocol; E-plates; Antigen-antibody detection; SPAG16.

ABSTRACT

Having an early diagnostic method would be beneficial to prevent autoimmune diseases from worsening. This is where Electrochemical Impedance Spectroscopy (EIS) biosensors become more promising in healthcare applications due to their ability to perform label-free measurements. Labels are, for example, enzymes attached to antigens. This will lead to a cost reduction and decrease in detection time of specific biomolecules. In addition, EIS can be applied in many other areas, including but not limited to: electrode redox reactions, power source applications, corrosion, and self-assembled monolayers. The aim of this paper is to assess whether it is possible to detect antigen-antibody interactions using an EIS biosensor. This was tested by optimizing an existing ELISA protocol. This protocol is based on studying the detection of Sperm-associated antigen 16 (SPAG16) with anti-SPAG16 antibody interactions. The experiments were performed on commercially available EIS biosensors as a proof of principle. Our results show that the EIS sensor can successfully detect SPAG-Thio antigen-antiSPAG antibody interactions. Currently, this sensor has a limit of detection of 100 pg/mL. However, non-specific interactions maintain a limitation of the sensor. It can be concluded that further research is required to reduce the non-specific interactions. This will result in a more optimized antigen-antibody detection. This is how we proved our proof of principle, which can be tested on homemade EIS sensors in a follow-up study.

INTRODUCTION

In the last few decades, significantly more people have been diagnosed with autoimmune diseases (ADs) like multiple sclerosis, rheumatoid arthritis, and psoriasis (1). Unfortunately there is no cure available yet for most ADs. Therefore, an early diagnosis is essential in order to prevent the disease from worsening. This can be achieved by detecting and monitoring specific biomarkers related to a particular AD using reliable methods (2). In this regard, an immunosensor is a well-studied method that has a variety of applications in clinical diagnostics (3, 4), but also in other fields such as food safety (5) and environmental monitoring (6).

An immunosensor is a type of biosensor that detects and quantifies a specific interaction between the target molecule (i.e., the analyte) and the antibody (Ab) in combination with a transducer that translates results into measurable signals (2, 7). These sensors are known to provide a highly sensitive and selective immunological response. They can provide real-time (i.e., as the surface binding occurs) measurements based on conventional immunoassay techniques (7, 8). Another attractive property of these sensors is that they can perform either label or label-free measurements. Avoiding labelling steps, results in a decreased detection time and cost reduction. Several immunosensors with different transducers have been developed, including optical, piezoelectric, and electrochemical devices (2, 7). Among them, electrochemical immunosensors are inexpensive and easy to miniaturize (9). Moreover, several electrochemical detection concepts have been studied throughout the years, including amperometric (10), potentiometric (11),

conductometric (12), and impedimetric immunosensors (13). Electrochemical impedance spectroscopy (EIS) is the focus of this paper.

The aim of this paper is to assess whether it is possible to detect antigen-antibody (Ag-Ab) interactions using an EIS immunosensor. It is hypothesized that the EIS sensor containing gold-coated interdigitated microelectrodes (IDEs) will be able to detect Sperm-associated antigen 16 (SPAG16) – antiSPAG antibodies. This will be studied by performing and further optimize an enzyme-linked immunosorbent assay (ELISA) protocol. ELISA is a quantitative analytical method in which an enzyme-linked conjugate and enzyme-substrate are used, resulting in a detectable signal by changing colour, which is readable by an optical transducer, indicating antigen-antibody reactions (7, 14). This study will use non-faradaic EIS biosensors to perform and further optimize a protocol based on the detection of SPag16–antiSPAG16 antibodies as a model application. The SPag16 is a sperm cell protein that also is present in the central nervous system (CNS) as an autoantibody target in the cerebrospinal fluid (CSF) and plasma of patients with multiple sclerosis, which is an AD (16, 17). This protocol will be examined with a commercially available EIS biosensor containing gold-coated IDEs as a proof of principle. After proving the proof of principle, this can be tested on homemade EIS sensors as a follow-up study.

WORKING PRINCIPLE

The mathematical concept of EIS was first introduced in the 1880s by Oliver Heaviside (18). In general, EIS is a technique that studies the electrical properties of electrode surfaces and binding kinetics between the electrolyte-electrode interface of biomolecules such as antigens (Ags), antibodies (Abs), DNA, proteins, etc. (19). The EIS method has been widely used in research for the detection of a variety of biomolecules (20). For example, Moulton et al. used this device to monitor the adsorption of HSA and IgG on gold electrodes (21). Z. Rashed et al. used an EIS-based biosensor to successfully detect SARS-CoV-2 antibodies (22). Besides biomolecules, EIS can also be used to study cells. For example, Hildebrandt et al. used an EIS to study the development of Human mesenchymal stem cells (23). Soley et al. used EIS to monitor the cell growth of yeast (24). Overall, EIS can be used for different types of studies such as interfacial processes (e.g. redox reactions at electrodes), applications in power sources (e.g. batteries), corrosion, self-assembled monolayers, sensors, etc. (25). For example, G Fernandez et al. used an EIS to monitor corrosion of low-Cr alloy steel T_{22} and high-Ni alloy HR_{224} in nitrate molten salt at a high temperature (26).

EIS is based on applying an alternative current (AC) potential with a small amplitude waveform, usually 5 - 10 mV, to the system of interest (e.g. sensor) (27). The applied AC potential has a sinusoidal waveform with a variable frequency (f) (Eq. 1), in which ω is the angular frequency (28).

$$f = \frac{\omega}{2\pi} \qquad \textbf{(Eq. 1)}$$

As a result, the response of an AC current as a function of the frequency is analysed (29). By applying Ohm's law (Eq. 2), the impedance (Z(ω,t) related to the system, which is the ratio of the voltage (V(ω,t)) to the current (I(ω,t)), can be calculated over a range of frequencies (usually from some MHz down to a few mHz) (27, 29). The impedance is a generalized resistance, i.e., it measures the ability of an electrical system to resist the electrical current flow (30). Moreover, unlike resistance, impedance **(a)** is frequency-dependent, **(b)** does not follow Ohm's law at all current and voltage levels, and **(c)** has AC current and voltage signals through a resistor which are not in phase with each other (30).

$$Z(\omega,t) = \frac{V(\omega,t)}{I(\omega,t)} \qquad \textbf{(Eq. 2)}$$

By applying Euler's relationship (Eq. 3), the impedance can be described as a complex function (Eq. 4) in terms of a magnitude |Z|, phase shift (Θ), a real part (Z'= |Z| cos Θ) and an imaginary part (Z" = |Z| sin Θ) (29). Here, the impedance magnitude and phase shift, which is the time difference between the transmitted AC voltage and the received current signal, can be calculated using equation 5 and 6 (29, 31). At the IMO-IMOMEC facility of UHasselt, impedance measurements of an EIS are usually performed using a well-known PalmSens4 portable potentiostat that is equipped with a frequency response analyser to measure the amplitude and phase shift (31).

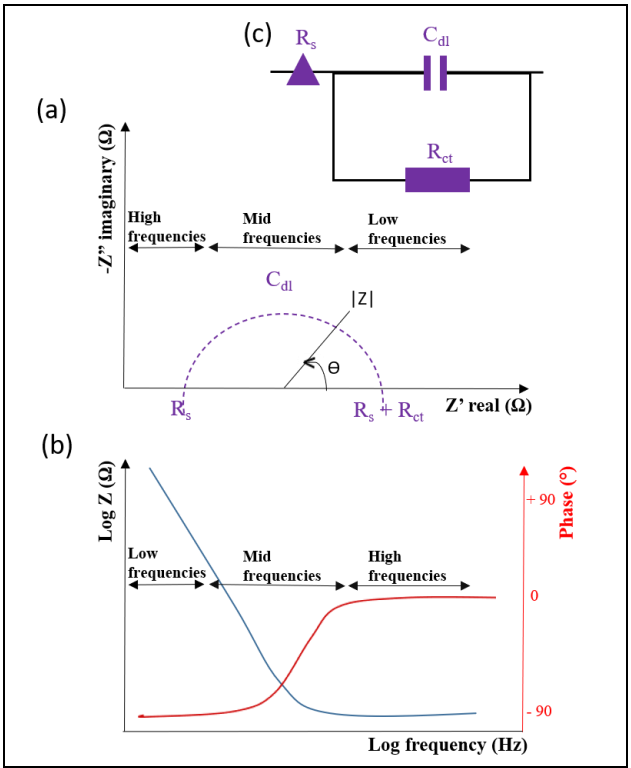

Fig. 1 – Graphical representation of a generalized (a) Nyquist plot and (b) Bode plot of a simple Randle circuit (c). R_s (solution resistance); C_{dl} (electrical double layer capacitance); R_{ct} (charge transfer resistance); Θ (phase shift); Ω (Ohm); ° (degree).

$$\text{Exp}(j\Theta) = \cos\Theta + j\sin\Theta \qquad \textbf{(Eq. 3)}$$

$$Z(\omega,t) = |Z(\omega)|(\cos\Theta + j\sin\Theta) = Z'(\omega) + jZ''(\omega) \qquad \textbf{(Eq. 4)}$$

$$|Z(\omega)| = \sqrt{Z'^2(\omega) + Z''^2(\omega)} \qquad \textbf{(Eq. 5)}$$

$$\Theta(\omega) = \tan^{-1}\left(\frac{Z''(\omega)}{Z'(\omega)}\right) \qquad \textbf{(Eq. 6)}$$

The EIS data are interpreted by fitting the electrochemical system under investigation into equivalent electrical circuit models. These circuits usually consist of series and parallel combinations of elements such as resistors and capacitors (15, 32). In this regard, the Randles circuit (Fig. 1c) is a wildly used model in which a simplified model of the total electrode impedance consists of a parallel connection of the electrical double layer capacitance (C_{dl}) and the charge transfer resistance (R_{ct}) in series with the solution resistance (R_s) (25, 33). These circuit elements will be explained throughout the following paragraph.

The EIS data of the electrochemical system under investigation can be presented into different graphical representations in which the Nyquist plot and Bode plot are commonly used (Fig. 1) (29, 34). On the one hand, a Nyquist plot (Fig. 1a), also referred to as a complex plane plot, is, in general, a plot of the negative imaginary impedance (y-axis) versus the real part of the impedance (x-axis) that is plotted for various frequencies (25, 35). The imaginary part contains information about the capacitance (explained further on) and phase shift, while the real part consists solely of a resistive component (36). For a simplified Randles cell, the Nyquist plot is observed as a semicircle (30). This being the case, at high frequencies, the applied signal is dominated by the R_s, which is frequency independent (37, 38). Thereby, the C_{dl} has a very low impedance which is close to zero (39). A C_{dl}, used to store charge (39), consists of a double layer that exists of opposite charges with oriented dipoles between the ions of the surrounding electrolyte (layer 1) and the charged metal electrode (layer 2) (30, 34). Moreover, these two layers are separated by an insulating space (= dielectric material), forming a capacitor (30). This insulating layer consists of solvent molecules and/or a film on the surface (36). Depending on several factors, such as the given electrode potential and ionic concentrations, the capacitor is usually in the range of 10-40 µF/cm^2 (30, 34). At low frequencies, the signal is dominated by the R_{ct} (37, 38). In other words, all the current goes through the R_{ct} (+ R_s) since the C_{dl} has a very high impedance at low frequencies (39). The R_{ct} is related to the back and forth movements of electrons in the electrode as a result of electrostatic interactions with ions in the solution (20, 34). At frequencies in between, also referred to as mid frequencies, the signal is mainly dominated by the C_{dl} at the electrode surface (38). Using equation 7, the C_{dl} can be calculated from the frequency at the highest point of the semicircle (39).

$$C_{dl} = \frac{1}{Rct * 2\pi * f(max)} \qquad \textbf{(Eq. 7)}$$

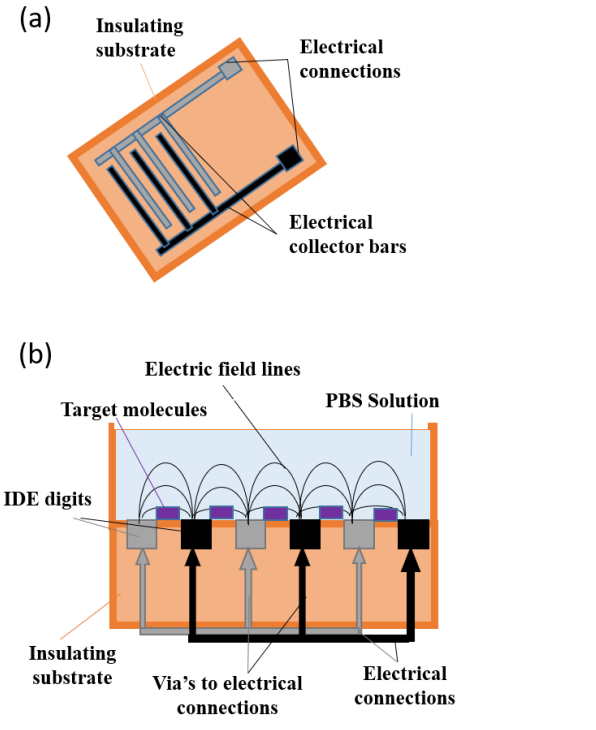

Fig. 2 – (a) planar IDE; (b) cross-section of planar IDE.

The Nyquist plot has the advantage of (a) being very sensitive to changes (39) and (b) allowing for an easy prediction of the above-mentioned circuit elements since they can be read directly from the plot (35, 39). However, one major disadvantage is that it's not possible to tell which frequency was used to record at any data point on the plot (30). On the other hand, a Bode plot (Fig. 1b) plots the logarithmic magnitude and the phase shift (y-axis) versus the logarithmic excitation frequency (x-axis) (25, 38). When observing the phase shift versus the log frequency, a capacitor in parallel to a resistor is visible as a peak (39) in which the phase angle changes from zero at high frequencies towards 90 degrees (90°) at low frequencies in case of an ideal electrode (35). Compared to the Nyquist plot, a bode plot has the advantage that it also includes frequency information (30).

EIS can be classified into faradaic or non-faradaic processes depending on the processes that take place at the electrodes. In the case of the faradaic process, the R_{ct} is the main parameter in which redox-active molecules are required in the solution. While the C_{dl} is the main parameter for non-faradaic processes, also referred to as capacitive sensors in which the sensing surface is covered by an insulating layer (15).

A standard electrochemical cell requires conductive electrodes and sample under test, which is usually solution-based (40). Thereby, a well-studied type of conductive electrodes is interdigitated microelectrodes (IDEs) (41). These electrodes are based on a pair of parallel array electrodes, which are comb-wise placed (Figure 2a) (38). As seen in Figure 2b, electric field line penetration occurs between adjacent electrodes of the planar-IDE sensor under an applied electrical potential. The effect of electric field lines on charged particles will result in an electric current signal (41).

EXPERIMENTAL PROCEDURES

EIS setup – The EIS setup consists of three components (Fig. 3a): (I) An impedance analyser (= palmSens4) sends a sinusoidal signal through (II) a multiplexer towards (III, Fig. 3c) a 16-well plate (commercially available RTCA E-plate, purchased from Agilent). The multiplexer is used to readout multiple channels at the same time, which can be connected to a maximum of 16 wells on the E-plate. The resulting current signal from the E-plate is sent back through the multiplexer towards the PalmSens4 (IV). Ohm's law (Eq. 2) is used to calculate the impedance of the system. Finally, (V) the data analysis is performed with a computer program (PalmSens4, PSTrace software). Fig. 3b is a picture of the used EIS setup equipment. A commercially available E-plate was used (Fig. 3c). This E-plate consists of 16 wells (Polystyrene) on top of an insulating substrate (Glass). The volume of each well is 270µL ± 10µl while the volume of the insulating substrate is 5.0mm ± 0.075mm. Gold-coated interdigitated electrodes (IDEs) (Fig. 2a) were used on the surface of each well.

ELISA protocol – An existing ELISA protocol (Fig. 4 and Supporting information (Table S1)) was used to perform EIS measurements for SPAG-Thio Ag – positive antiSPAG Ab detection as follows. Step I: EIS measurement was performed on blank wells in a 1x Phosphate-buffered saline (1x PBS buffer solution) (0.1M sodium phosphate, 0.15M sodium chloride, pH 7.2) for 15 sweeps at room temperature (20 °C). This was used as a baseline for the whole measurement. Step II: 1x PBS buffer solution was pipetted out of the blank

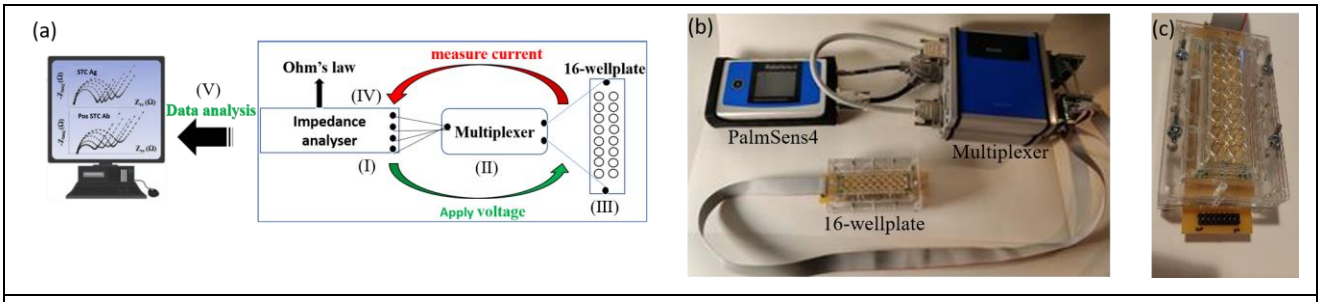

Fig. 3 – (a) Schematic representation of the EIS setup (steps I -V). (b) Picture of the EIS setup equipment. (c) Close-up photo of the 16-well plate (E-plate).

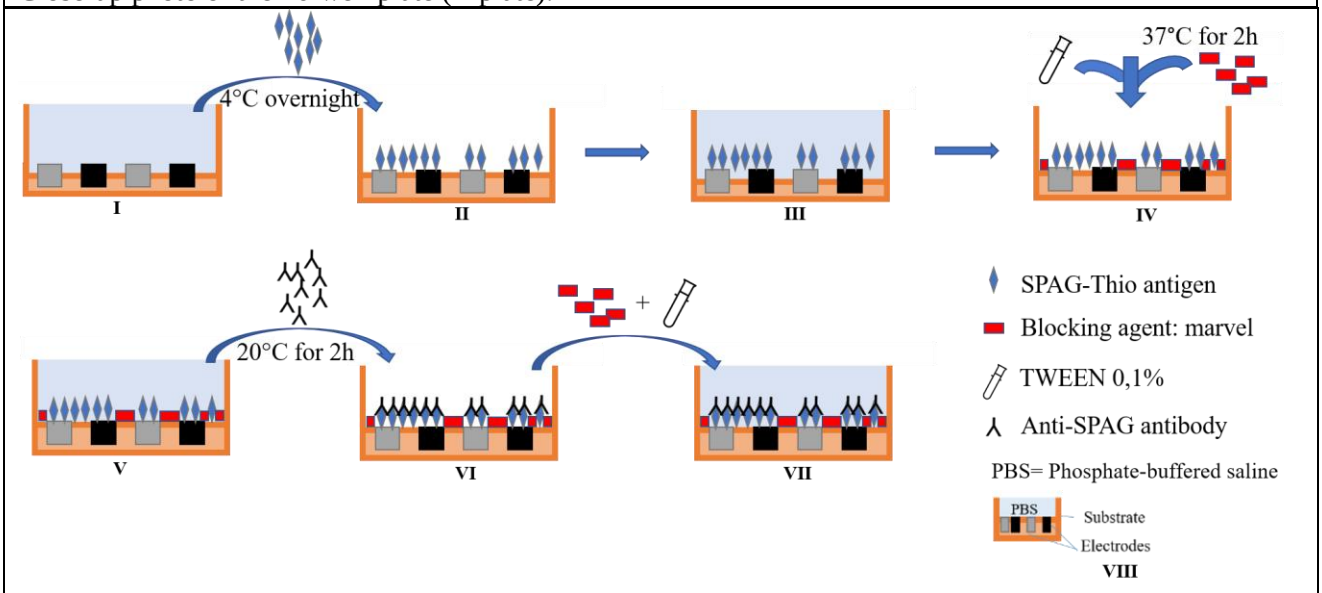

Fig. 4 – Schematic representation of the ELISA protocol (steps I - VII) with (VIII) the legend.

wells and was coated with SPAG-Thio Ags (in-house made) medium overnight at 4 °C. SPAG-Thio Ags are sticky, which will cover the whole well surface. Excessive SPAG-Thio medium was washed away by flushing the wells 5x with 1x PBS. This was followed by an EIS measurement of the SPAG-Thio coated wells in a 1x PBS buffer solution for 15 sweeps at room temperature (20 °C) (step III). Step IV: 1x PBS buffer solution was pipetted out of the SPAG-Thio coated wells and was coated with a blocking agent (mixture of 2% Marvel skimmed milk in 1x PBS buffer solution) for 2 h at 37 °C to fill up the non-occupied zones. Excessive blocking agent was washed away with Tween (mixture of Tween (0.1%) in 1x PBS, Fisher bioreagents) into the wells for 5 minutes at room temperature (20 °C). This was followed by an extra washing step with 1x PBS. Step V: A real-time measurement was started of the SPAG-Thio, and blocking agent coated wells in a 1x PBS buffer solution for 15 sweeps. Next, the real-time measurement was paused. 1x PBS buffer solution was pipetted out of the wells and was coated with positive antiSPAG Abs (plasma from different donors) medium in which the real-time measurement continued for 2 h at room temperature (20 °C) (step VI). Step VII: The measurement was paused for a second time. Excessive positive antiSPAG Ab medium was pipetted out of the wells and was washed out with blocking agent (2%) for 5 minutes, followed by Tween (0.1%) for 5 minutes at room temperature (20 °C). Finally, the real-time measurement of the Ag-Ab coated wells continued in a 1x PBS buffer solution for 15 sweeps at room temperature (20 °C). For measurements performed with Thio Ags (in-house made), Thio Ag medium was used instead of SPAG-Thio Ag medium. For measurements performed with negative SPAG Abs (plasma from different donors), negative SPAG Ab medium was used instead of positive SPAG Ab medium.

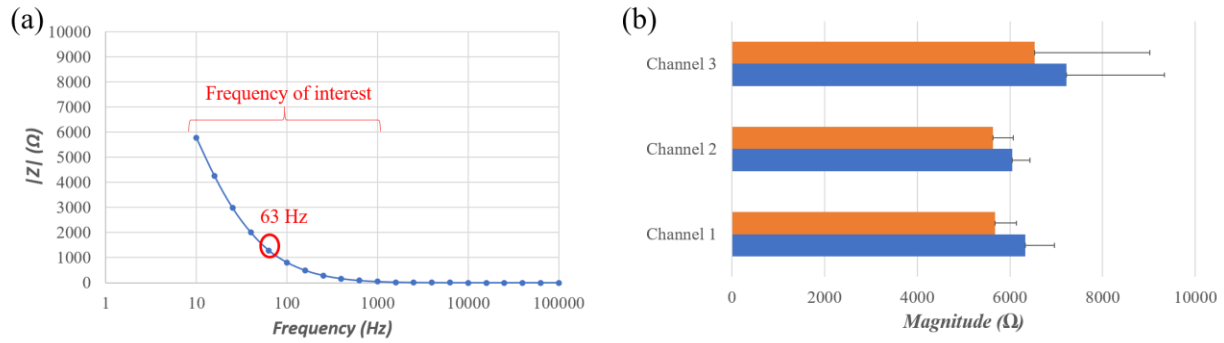

Fig. 5 – (a) Bode plot representing the frequencies of interest (10-10^5 Hz). 63 Hz was used for further data analysis. (b) Bar graph representing Ag detection on the EIS sensor electrodes. Three channels are presented, performed during one measurement. Experimental conditions: Orange: before STC Ag; Blue: after STC Ag (1200 µg/mL). For all conditions, the magnitude was taken from 63 Hz. Results are presented as average ± SD (n = 4).

Data analysis procedure – EIS measurements were used to characterize the commercially available sensor electrodes, as well as to measure Ag-Ab detection on gold-coated IDEs. EIS measurements were carried out using a voltage in the frequency range 10-10^5 Hz with 10mV amplitude using a PalmSens4 potentiostat, controlled by PSTrace software (version 5.8, PalmSens4). Twenty-one frequencies with five data points were measured per sweep. A total of 15 sweeps were executed per measurement. All measurements were performed at room temperature (20 °C), unless indicated otherwise (protocol section). This data was further analysed using an in-house made EIS analysis platform (Python, IMO-IMOMEC). Excel was used to analyse the raw data to create bode plots and bar graphs. The average ± standard deviations (SD) of the bar graphs were calculated using Excel software.

RESULTS and DISCUSSIONS

EIS sensor electrode characterization – In order to test for Ag-Ab detection, a commercially available biosensor was used as a proof of principle (M&M section). All assumptions made in the 'results and discussions section' are based on the authors' analysis. Prior to testing the hypothesis, Ag detection on the sensor electrodes was assessed (Fig. 5). This was done by analysing the data after SPAG-Thio Ag coating (STC Ag) versus before STC Ag. The sensor surface alteration between both was analysed by studying the raw data using a bar graph representation (Fig. 5b). First, a bode plot (Fig. 5a) was used to assess at which frequencies an alteration of the magnitude impedance could be detected for STC Ag, representing the C_{dl}. Therefore, the average of 10 sweeps after STC Ag was subtracted from the average of 10 sweeps before STC Ag from the magnitude for all frequencies (10-10^5 Hz). Fig. 3a shows that the frequencies of interest are between 10 Hz and 1000 Hz because, at these frequencies, the magnitude is frequency-dependent. While at higher frequencies, the magnitude decreases, followed by a constant region. At this moment, the magnitude is frequency independent. This is in agreement with the findings of Guimerà A. et al., who states that the bode plot signal at lower frequencies is mainly dominated by the C_{dl} (41). Next, a bar graph (Fig. 5b) was created to clearly visualize the difference in impedance after STC Ag (1200 µg/mL) versus before STC Ag. Therefore, the average of 10 sweeps was taken from the magnitude at a frequency of 63 Hz. For the bar graph, only one frequency (63 Hz) of interest was used as a reference. This was done for the raw data of both, after STC Ag and before STC Ag. Moreover, three channels during each measurement were studied. These channels represent the average of four different measurements for each channel to emphasize reproducibility. Our results show a higher magnitude after STC Ag compared to the magnitude before STC Ag. A consistent magnitude can be observed between the three channels. The magnitude ± SD before STC Ag is: channel 1 = 5675 Ω ± 463; channel 2 = 5633 Ω ± 437 and channel 3 = 6533 Ω ± 2485. The magnitude ± SD after SPC Ag is: channel 1 = 6327 Ω ± 633; channel 2 = 6052 Ω ± 380 and channel 3 = 7218 Ω ± 2111.

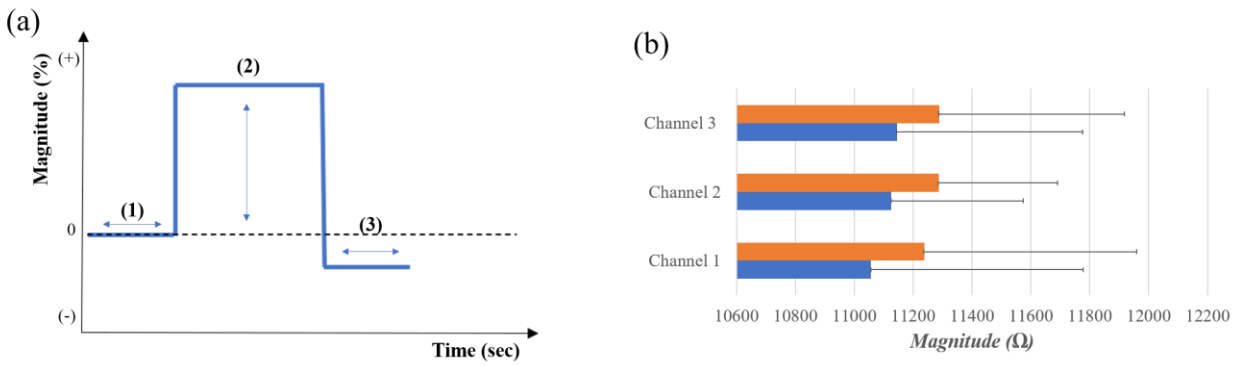

Fig. 6 – (a) Time graph: (1) before Pos antiSC Ab, (2) during Pos antiSC Ab, and (3) after Pos antiSC Ab. The Time graph represents the magnitude at one frequency of interest (10 Hz – 1000 Hz). (b) Bar graph representing Ab detection. Three channels are presented, performed during one measurement. Experimental conditions: Orange: before Pos antiSC Ab; Blue: after Pos antiSC Ab (0.1 µg/mL). Abs were tested on STC Ags (1200 µg/mL). For all conditions, the magnitude is taken from 63 Hz. Results are presented as average ± SD (n =3).

This indicates Ag detection on the sensor electrodes since a clear difference of the sensor surface after versus before STC Ag is observed. It can also be noticed that the PBS buffer solution results in a certain magnitude impedance. A possible explanation is that during the performance of the measurements, the ions which are present in PBS at a certain pH tend to sediment on the surface of the sensor electrodes. This can be seen as an insulating layer, i.e., the C_{dl} increases. As a result, an increased impedance to the flowing current occurs. On the other hand, the higher impedance that is observed after STC Ag is as expected because the sedimented Ags form a larger C_{dl} compared to the ions of the PBS. This way, the voltage at a certain frequency needs to cross a higher path which results in an increased magnitude impedance.

Antibody detection – After the characterization of the sensor electrodes in which we proved that our sensor can successfully detect Ag coating, antibody detection was assessed. This was done by analysing the data after positive antiSPAG Ab coating (Pos antiSC Ab) (0.1 µg/mL) versus before Pos antiSC Ab on STC Ags (1200 µg/mL) (Fig. 6). The sensor surface alteration between both was analysed by studying the raw data using a bar graph representation (Fig. 6b). First, a time graph was analysed to study the alteration of the difference in magnitude percentage over time, after versus before Pos antiSC Ab at one frequency of interest (between 10 Hz and 1000 Hz) (Fig. 6a). This graph is a graphical representation of what is expected to happen with the magnitude percentage based on our results. All expectations in this paragraph are based on the time graph results of the measurements we performed. This time graph consists of three regions: 1, 2, and 3. Before Pos antiSC Ab, the E-plate wells only contains STC Ags. At this moment, real-time measurements are being performed in a 1x PBS buffer solution. This is expected to be observed at the time graph as region 1, in which the magnitude percentage remains constant over time. During Pos antiSC Ab, real-time measurements are being performed in a Pos antiSC Ab buffer solution instead of a 1x PBS buffer solution. This is expected to be observed at the time graph as region 2, in which an increase of the impedance, followed by a constant phase, overtime is noticed. Finally, after Pos antiSC Ab, real-time measurements are again being performed in a 1x PBS buffer solution. This is expected to be observed at the time graph as a constant with a lower impedance over time compared to region 1. These observations will be discussed later on at the end of this paragraph. Next, a bar graph was used to clearly visualize the difference in impedance after Pos antiSC Ab versus before Pos antiSC Ab (Fig. 6b). Therefore, the average of 10 sweeps was taken from the magnitude at a frequency of interest (63 Hz). This was done for the raw data of both, after Pos antiSC Ab and before Pos antiSC, which was studied for three channels during one measurement. These channels represent the average

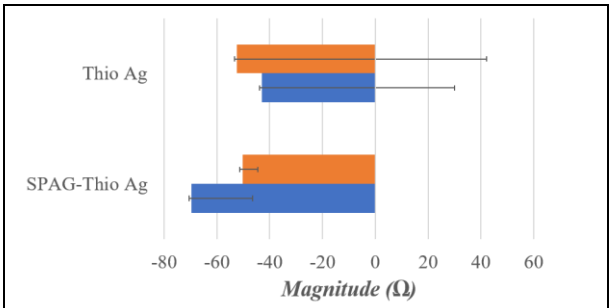

Fig. 7 – Bar graph representing the EIS sensor specificity. Experimental conditions: Blue: Pos antiSC Ab (0.1 µg/mL); Orange: Neg antiSC Ab (0.1 µg/mL). Abs were tested on STC Ags (1200 µg/mL) and TC Ags (965.6 µg/mL). For all conditions, the magnitude is taken from 100 Hz. Results are presented as average ± SD (n = 2).

of three different measurements for each channel to emphasize reproducibility. Our results show a lower magnitude after Pos antiSC Ab compared to the magnitude before Pos antiSC Ab. A consistent result can be observed between the three channels. The magnitude ± SD before Pos antiSC Ab is: channel 1 = 11237 Ω ± 722; channel 2 = 11286 Ω ± 405 and channel 3 = 11288 Ω ± 630. The magnitude ± SD after Pos antiSC Ab is: channel 1 = 11057 Ω ± 721; channel 2 = 11126 Ω ± 449 and channel 3 = 11145 Ω ± 631. These results indicate that Pos antiSC Ab can be successfully detected with our EIS sensor. Taken into account both graphs, Fig. 6a and Fig. 6b, the following can be discussed, based on the observations of the author. A possible explanation for the three regions with a different magnitude percentage (Fig. 6a) can be explained as follows. During the real-time measurements in region 1, there is already a C_{dl} available at the surface of the sensor electrodes. This C_{dl} consists of sedimented STC Ags and a blocking agent. As a consequence, the sedimentation of the ions of the PBS on this C_{dl} will have a negligible influence on the impedance. While in region 2, sedimented Pos antiSC Abs interact with the STC Ags. This creates a bigger C_{dl} over time, which forces the voltage at frequencies of interest to bridge a longer path, thereby increasing the magnitude impedance. In conclusion, the Pos antiSC Ab buffer solution leads to a higher magnitude compared to the PBS buffer solution, which can be observed in the transition between region (1-2) and region (2-3). Finally, the lower impedance in region three versus region 1 of Fig. 6a possibly suggests that the Pos antiSC Abs behave more as electrical conductive molecules, thereby reducing the impedance, which is also seen in Fig. 6b. While the STC Ags behave more as electrical resistive molecules. This means that a higher magnitude is expected to be observed before Pos antiSC Abs.

Sensor specificity test – Now that it has been proven that our sensor can successfully detect Ag-Ab reactions, this paragraph will discuss the specificity of the sensor. Two methods have been proposed for the determination of how specific these Ag-Ab reactions occur on the sensor surface. For the first specificity test method, Pos antiSC Ab (0.1 µg/mL) was compared with negative antiSPAG Ab Coating (Neg antiSC Ab) (0.1 µg/mL) on STC Ags (1200 µg/mL) (Fig 7). The difference between both is that Pos antiSC Abs react with the STC Ags. At the same time, Neg antiSC Abs do not react with the STC Ags. As a result, it is expected that the Neg antiSC Ab will be washed away after the Tween cleaning step while most of the Pos antiSC Ab should remain interacted with the STC Ags. Consequently, these Pos antiSC Ags should result in a decreased amplitude as already has been proven (Antibody detection section). While for the Neg antiSC Ab, a magnitude of ± 0 Ω is expected since most of these Abs should be washed away after Neg antiSC Ab. The sensor surface alteration between both was analysed by studying the raw data using a bar graph representation (Fig. 7). Therefore, the average of 10 sweeps after Pos antiSC Ab was subtracted from the average of 10 sweeps before Pos antiSC Ab. This was done for the magnitude at a frequency of interest (100 Hz). The same was executed for the raw data of the Neg antiSC Ab. Fig. 7 represents the average of the magnitude of two different measurements to emphasize reproducibility. The magnitude ± SD of Pos antiSC Ab and Neg antiSC Ab on STC Ags is respectively -70 Ω ± 23 and -50 Ω ± 6. These results show that after Pos as well as Neg antiSC Abs, a reduced magnitude is observed when compared to the magnitude before Pos and Neg antiSC Ab. This has already been discussed earlier (Antibody detection section). Based on this discussion, it can be concluded that also the Neg antiSC Abs behave as electrical conductive

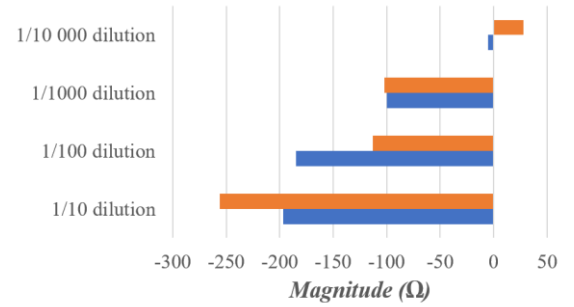

Fig. 8 – Bar graph representing the analytical performance of the EIS sensor. Experimental conditions: Blue: Pos antiSC Ab; Orange: Neg antiSC Ab. Abs were tested on STC Ags (1200 µg/mL). Four dilutions (1/10, 1/100, 1/1000, and 1/10 000) of Pos and Neg antiSC Abs were used during one measurement. For all conditions, the magnitude was taken from 63 Hz. Results are presented as one measurement.

molecules, which results in a decreased magnitude. Furthermore, it can be noticed that Pos antiSC Ab has a more negative impedance when compared to the Neg antiSC Abs. This suggests that Pos antiSC Abs result in a lower impedance to the flowing current between the electrodes. A possible explanation for this is that specific bindings occur between Pos antiSC Ab and STC Ags. This will create a bigger C_{dl}. Taking into account that these Pos antiSC Abs behave as electrical conductive molecules, an increased negative magnitude can be expected. On the other hand, as already explained before, Neg antiSC Abs should not interact with STC Ags. However, the negative magnitude that is observed in Fig. 7 possibly indicates the occurrence of non-specific interactions between Neg antiSC Abs and STC Ags. These non-specific interactions can account for different types of interactions, such as ionic interactions, Van der Waals forces, and weak electrostatic interactions between dipolar molecules (42). This being the case, the non-specific interactions will cause only part of the Neg antiSC Abs to interact with the STC Ags, while the non-interact part will be washed away during the Tween cleaning step. This way, only the interacted part will contribute to a bigger C_{dl}. As a result, these electrical conductive Neg antiSC Abs will have a slightly higher impedance to the flowing current compared to Pos antiSC Abs. This is reflected in Fig. 7 by means of having a lower negative magnitude compared to the Pos antiSC Abs.

For the second specificity test method, the difference in the interaction of Pos and Neg antiSC Abs on STC Ags was compared to the difference in the interaction of Pos and Neg antiSC Abs on Thio coating Ags (TC Ags) (965.6 µg/mL) (Fig 7). In this case, it is expected that both Abs will result in non-specific interactions to the TC Ags. This specificity test method was performed in parallel with the first specificity test method on different wells from the same E-plate. Therefore, the same data analysis was performed as explained for the first specificity test method. The magnitude ± SD of Pos antiSC Ab and Neg antiSC Ab on TC Ags is respectively – 42 Ω ± 73 and -52 Ω ± 95. These results show that Pos antiSC Abs on TC Ags have a less negative impedance when compared to the Neg antiSC Abs. This suggests that Pos antiSC Abs result in a higher impedance to the flowing current between the electrodes. A possible explanation for this is that this time, non-specific interactions occur between Pos antiSC Ab and TC Ags, compared to the interactions on STC Ags. This will create a smaller C_{dl} compared to interactions between Pos antiSC Ab and STC Ags, which can be noticed in Fig. 7. The same can be concluded for interactions occurring between Neg antiSC Ab and TC Ags as already explained for the first specificity test method in which Neg antiSC Ab interacted on STC Ags. However, Fig. 7 shows a slightly more negative magnitude for the Neg antiSC Abs in comparison to the Pos antiSC Abs on TC Ags. This suggests that Neg antiSC Abs result in more non-specific interactions with the TC Ags.

Evaluation of the analytical performance of the sensor – After proving that our EIS sensor is more specific towards Pos antiSC Ab – STC Ag interactions while still maintaining non-specific interactions, this paragraph will discuss the analytical performance of the sensor. This was done by assessing decreasing concentrations of Pos as well as Neg antiSC Abs on STC Ags (1200 µg/mL). These concentrations consisted of four dilutions (1/10, 1/100, 1/1000, and 1/10 000). The raw data analysis for both was performed by subtracting the average of 10 sweeps after antiSC Ab from the average of 10 sweeps before antiSC Ab (Fig 8). The data were analysed for one measurement. The magnitude of the Pos antiSC Ab dilutions on STC Ags is: 1/10 = –197 Ω; 1/100 = –185 Ω; 1/1000 = –100 Ω and 1/10 000 = –5. The magnitude of the Neg

antiSC Ab dilutions on STC Ags is: 1/10 = –256 Ω; 1/100 = –113 Ω; 1/1000 = –102 Ω and 1/10 000 = +28 Ω. These results show that a lower concentration of Pos and Neg antiSC Ab results in a less negative magnitude. A feasible explanation is that a higher Ab dilution results in less Ag-Ab interaction on the sensor surface. Thereby, the C_{dl} will only increase with a small amount, depending on the attached Abs to the STC Ags. As a consequence, a higher dilution of electrical conductive Abs will have less contribution towards the flowing current between the electrodes when compared to lower Ab dilutions. This can be seen in Fig. 8 as a less negative magnitude. Moreover, it can be noticed that a Pos antiSC Ab dilution of 1/10 000 (100 pg/mL Pos antiSC Ab) can still be detected by our sensor. It should be pointed out that 1/10 000 is the lowest dilution tested, as our lab was unable to produce lower Ab dilutions. Based on the discussion in the 'sensor specificity test' section and the results of Fig. 8, it can be concluded that a limitation of our EIS sensor remains the unintended consequence of non-specific interactions.

CONCLUSION AND OUTLOOK

In this study, a commercially available EIS biosensor with gold-coated IDE has been assessed for the detection of Ag-Ab interaction. It has been proven that this sensor can successfully detect Ag-Ab interactions. Thereby, STC Ags/Pos SC Abs were used as model biomolecules. Furthermore, a more specific interaction is observed towards Pos antiSC Abs on STC Ags compared to Neg antiSC Abs. On the other hand, a limitation of this sensor is the occurrence of non-specific interactions, which is a limiting factor for optimal sensor detection. Taken together, these results show that the EIS sensor is able to detect Ag-Ab interactions, but it still needs some improvements to reduce the non-specific interactions. This limitation should be further studied in a follow-up study. Therefore, instead of using Marvel as a blocking agent, different types of blocking agents can be used during the performance of this ELISA protocol. The to be tested blocking agents include bovine serum albumin (BSA), whole normal serum, fish gelatin, and non-fat dry milk. After proving the proof of principle, the improved ELISA protocol can be tested on homemade EIS biosensors as a follow-up study. The surface of this prototype sensor contains larger-sized IDEs, which makes it easier to verify Ag-Ab interactions using a microscope and a contact angle measurement. The final step is to improve the equivalent circuit of the current planar-IDE EIS sensor. This device will contain insulating barriers between the IDE digits, which are referred to as 3D-IDEs. It is expected that the electric current will become more concentrated on the surface conductivity layer. Our research team's expectation is that this will increase the sensitivity of the sensor. Finally, statistical principal component analysis (PCA) will determine the most relevant parameters of the sensor based on a simple equivalent circuit model. With this, we hope to transfer this technology platform to similar electrochemical impedance-based immunosensors and other types of sensors such as thermal sensors or a combination of impedance and thermal sensors, which focus on detecting other relevant Ag-Ab reactions.

Acknowledgments – AMOO, would like to thank Prof. dr. ir Thoelen Ronald, Drs. eng. Bormans Seppe and Drs. eng. Vandenryt Thijs for giving me the opportunity to work under their supervision. AMOO acknowledges and is grateful for the help of Dusaer Laura and Dr. Slaets Leen that they provided by applying us with all the required materials for the protocol.

Author contributions – TR, BS, and VT conceived and designed the research. AMOO performed experiments and data analysis. AMOO wrote the paper. All authors carefully edited the manuscript.

REFERENCES

1. Parliament. E. Directorate-General for Internal Policies: Autoimmune Disease—Modern Diseases. . 2017.
2. Florea A, Melinte G, Simon I, Cristea C. Electrochemical Biosensors as Potential Diagnostic Devices for Autoimmune Diseases. Biosensors (Basel). 2019;9(1).
3. San L, Zeng D, Song S, Zuo X, Zhang H, Wang C, et al. An electrochemical immunosensor for quantitative detection of ficolin-3. Nanotechnology. 2016;27(25):254003.
4. Lopes P, Costa-Rama E, Beirao I, Nouws HPA, Santos-Silva A, Delerue-Matos C. Disposable electrochemical immunosensor for analysis of cystatin C, a CKD biomarker. Talanta. 2019;201:211-6.
5. Selvakumar LS, Thakur MS. Dipstick based immunochemiluminescence biosensor for the analysis of vitamin B12 in energy drinks: a novel approach. Anal Chim Acta. 2012;722:107-13.
6. Gallardo-Carreno I, Moreno-Paz M, Aguirre J, Blanco Y, Alonso-Pintado E, Raymond-Bouchard I, et al. A Multiplex Immunosensor for Detecting Perchlorate-Reducing Bacteria for Environmental Monitoring and Planetary Exploration. Front Microbiol. 2020;11:590736.
7. Mollarasouli F, Kurbanoglu S, Ozkan SA. The Role of Electrochemical Immunosensors in Clinical Analysis. Biosensors (Basel). 2019;9(3).
8. Ahn KC, Kim HJ, McCoy MR, Gee SJ, Hammock BD. Immunoassays and biosensors for monitoring environmental and human exposure to pyrethroid insecticides. J Agric Food Chem. 2011;59(7):2792-802.
9. Felix FS, Baccaro ALB, Angnes L. Disposable Voltammetric Immunosensors Integrated with Microfluidic Platforms for Biomedical, Agricultural and Food Analyses: A Review. Sensors (Basel). 2018;18(12).
10. Zhou X, Li Y, Wu H, Huang W, Ju H, Ding S. A amperometric immunosensor for sensitive detection of circulating tumor cells using a tyramide signal amplification-based signal enhancement system. Biosens Bioelectron. 2019;130:88-94.
11. Silva NFD, Almeida CMR, Magalhaes J, Goncalves MP, Freire C, Delerue-Matos C. Development of a disposable paper-based potentiometric immunosensor for real-time detection of a foodborne pathogen. Biosens Bioelectron. 2019;141:111317.
12. Hnaiein M HW, Abdelghani A, Fournier-Wirth C, et.all. . A conductometric immunosensor based on functionalized magnetite nanoparticles for E. coli detection. . 2008.
13. Chinnadayyala SR, Park J, Abbasi MA, Cho S. Label-free electrochemical impedimetric immunosensor for sensitive detection of IgM rheumatoid factor in human serum. Biosens Bioelectron. 2019;143:111642.
14. Aydin S. A short history, principles, and types of ELISA, and our laboratory experience with peptide/protein analyses using ELISA. Peptides. 2015;72:4-15.
15. Zamfir LG, Puiu M, Bala C. Advances in Electrochemical Impedance Spectroscopy Detection of Endocrine Disruptors. Sensors (Basel). 2020;20(22).

16. de Bock L SK FJ, Hendriks JJA, van Horssen J, Rouwette M, et al. Sperm-associated antigen 16 is a novel target of the humoral autoimmune response in multiple sclerosis. 2014.
17. de Bock L, Fraussen J, Villar LM, Alvarez-Cermeno JC, Van Wijmeersch B, van Pesch V, et al. Anti-SPAG16 antibodies in primary progressive multiple sclerosis are associated with an elevated progression index. Eur J Neurol. 2016;23(4):722-8.
18. O. H. Electrical papers: New York and London : Macmillan and co.; 1894.
19. Deniz ErtuğruL H OUZ. Impedimetric Biosensors for Label-Free and Enzymless Detection.2013.
20. Manickam A, Johnson CA, Kavusi S, Hassibi A. Interface design for CMOS-integrated Electrochemical Impedance Spectroscopy (EIS) biosensors. Sensors (Basel). 2012;12(11):14467-88.
21. Moulton SE, Barisci JN, Bath A, Stella R, Wallace GG. Investigation of protein adsorption and electrochemical behavior at a gold electrode. J Colloid Interface Sci. 2003;261(2):312-9.
22. Rashed MZ, Kopechek JA, Priddy MC, Hamorsky KT, Palmer KE, Mittal N, et al. Rapid detection of SARS-CoV-2 antibodies using electrochemical impedance-based detector. Biosens Bioelectron. 2021;171:112709.
23. Hildebrandt C I, Thielecke H. Non-invasive Characterization of the Osteogenic Differentiation of hMSCs in 3D by Impedance Spectroscopy. 2009.
24. Soley A, Lecina M, Gamez X, Cairo JJ, Riu P, Rosell X, et al. On-line monitoring of yeast cell growth by impedance spectroscopy. J Biotechnol. 2005;118(4):398-405.
25. A. L. Electrochemical Impedance Spectroscopy and its Applications.2014.
26. Fernandez AG MA. Corrosion Monitoring by Electrochemical Impedance Spectroscopy Test of LowCr Alloy Steel T22 and High-Ni Alloy HR224 in Nitrate Molten Salt. 2018.
27. AW. B. Electrochemical techniques for the characterization of redox polymers. 2001.
28. A. S. Electrochemical impedance spectroscopy as a tool to investigate the electroreduction of carbon dioxide: A short review. 2018.
29. A. S. Electrochemical impedance spectroscopy: Fundamentals and application indye-sensitized solar cells. 2017.
30. Instruments. G. Basics of Electrochemical Impedance Spectroscopy. 2021 [Available from: https://www.gamry.com/application-notes/EIS/basics-of-electrochemical-impedance-spectroscopy/.
31. Palmsens. Frequency response analyzer 2021 [Available from: https://www.palmsens.com/frequency-response-analyzer/.
32. Duchateau S BJ, Croux D, Janssen D, et.all. Cell proliferation monitoring by multiplexed electrochemical impedance spectroscopy on microwell assays. 2013.
33. Lisdat F SD. The use of electrochemical impedance spectroscopy for biosensing. 2008.
34. Bard AJ FL. ELECTROCHEMICAL METHODS Fundamentals and Applications. 2nd ed. ed2001.
35. A. L. Electrochemical Impedance Spectroscopy and its Applications.1999.
36. L. B. EIS 101, an introduction to electrochemical spectroscopy. 2015.
37. Randviir EP BC. Electrochemical impedance spectroscopy: an overview of bioanalytical applications. 2013.
38. Leva-Bueno J, Peyman SA, Millner PA. A review on impedimetric immunosensors for pathogen and biomarker detection. Med Microbiol Immunol. 2020;209(3):343-62.
39. Palmsens. Bode and Nyquist Plot. 2021 [Available from: https://www.palmsenscorrosion.com/knowledgebase/bode-and-nyquist-plot/.

40. Jin K, Hu S, Su Y, Yang C, Li J, Ma H. Disposable impedance-based immunosensor array with direct-laser writing platform. Anal Chim Acta. 2019;1067:48-55.
41. Guimerà A. P-AE, et.all. . Effect of surface conductivity on the sensitivity of interdigitatedimpedimetric sensors and their design considerations. . 2014.
42. Systems RD. Preventing Non-specific Staining [Available from: https://www.rndsystems.com/resources/protocols/preventing-non-specific-staining.

SUPPORTING INFORMATION

Table 1 – ELISA protocol. PBS (1x Phosphate-buffered saline), Ags (antigens) Abs (antibodies)

	Temperature (°C)	Medium	Contents	Duration of the step
Step I	20	1X PBS	/	15 sweeps
Step II	4		**SPAG-Thio Ags**	2 hours
Step III	20	1X PBS	/	15 sweeps
Step IV	37	1X MPBS (2%)	**Blocking: Marvel skimmed milk**	2 hours
	20	1X PBST	**(Tween 0.1%)**	5 minutes
Step V	20	1X PBS	/	15 sweeps
Step VI	20		**Analyte: Pos antiSPAG Abs**	2 hours
Step VII	20	1X MPBS (2%)	**Blocking: Marvel skimmed milk**	5 minutes
	20	1X PBST	**Tween (0.1%)**	5 minutes
	20	1X PBS	/	15 sweeps